Generation of broadband optical chaos at mid-infrared wavelength with an interband cascade laser

O. Spitz,[1, a)] Y. B. Shuai,[2] S. Zhao,[1] P. Didier,[1, b)] D. A. Díaz-Thomas,[3] A. N. Baranov,[3] L. Cerutti,[3] D. Rontani,[4] J. Wu,[2] and F. Grillot[1, c)]

[1)] *LTCI Telecom Paris, Institut Polytechnique de Paris, 19 Place Marguerite Perey, Palaiseau 91120, France*

[2)] *School of Physical Science and Technology, Southwest University, Chongqing, 400715, China*

[3)] *Institut d'Electronique et des Systèmes, Université de Montpellier, CNRS UMR 5214, Montpellier, 34000, France*

[4)] *Chair in Photonics, LMOPS EA 4423 Laboratory, CentraleSupélec & Université de Lorraine, Metz, 57070, France*

(*Electronic mail: olivier.spitz@ucf.edu.)

(Dated: 18 April 2024)

Nonlinear dynamics at mid-infrared wavelength is of interest for various applications but has been mainly limited to quantum cascade lasers so far. In this article, we show that interband cascade lasers can generate complex optical chaos with bandwidth in the GHz range and this outperforms the performances of quantum cascade laser chaos. The chaos nature of our signal is confirmed by a thorough time-series analysis. Modelling of the semiconductor laser under short-cavity external optical feedback allows confirming the high-bias chaos operation that we observe experimentally. These results pave the way for applications at mid-infrared wavelength, such as private free-space communication.

I. INTRODUCTION

A wide variety of mid-infrared nonlinear dynamics has been exhibited experimentally[1] since the demonstration of quantum cascade photonic chaos in 2016.[2] Quantum cascade lasers (QCLs) are semiconductor lasers of choice for those phenomena, and applications such as chaos-based communication are now available in this wavelength domain.[3] Yet, most of the nonlinear dynamics observed in quantum cascade lasers have a limited bandwidth,[4,5] despite the intersubband technology of QCLs. This limited bandwidth converts into a limited transmission rate in the case of chaos-based communication. In order to circumvent this limitation, we decided to explore mid-infrared nonlinear dynamics in another structure called interband cascade lasers (ICLs). These lasers rely on cascaded interband technology, which means that a sequence of quantum wells in a designed cascade heterostructure allows achieving stimulated emission at mid-infrared wavelength, and they exhibit relaxation oscillations in the range of GHz, as demonstrated numerically[6] and experimentally.[7] They are promising optical sources for various mid-infrared applications such as greenhouse gases monitoring[8,9] and quantum sensing.[10,11]

Recently, it has been shown experimentally[12] that ICLs can generate hyperchaos, which is chaos characterized by several positive Lyapunov exponents,[13] and simulation showed promising dynamics bandwidth,[6] though the influence of the number of stages on the dynamics behavior still needs to be investigated experimentally. The hyperchaos bandwidth in ICLs is typically one order of magnitude larger than that found experimentally in QCLs. Consequently, ICLs are relevant for high-speed applications relying on optical chaos. Apart from the aforementioned chaos-based communication, optical nonlinear dynamics were proven useful in chaotic LiDARs with near-infrared wavelength semiconductor lasers, which are of interest for low-cost deployment and eye-safe operation.[14] The high-speed complex dynamics and the fast-decaying autocorrelation function ensure a high-precision, reliable detection system with a maximum range of several meters and precision below one centimeter.[15] Optical chaos has also been harnessed for physical random bit generation (RBG). This method was introduced in 2009 by sampling the fluctuating optical output of two chaotic lasers for RBG at 1.7 Gbps[16] and this seminal paper led to many demonstrations in the Gbps range in the following years.[17–19] Subsequent improvements have paved the way towards Tbps RBG,[20–23] and a recent experimental effort taking advantage of spatio-temporal dynamics in a broad-area semiconductor laser has achieved the record rate of 250 Tbps.[24]

In this work, we show that an interband cascade laser emitting at 4.1 μm can generate complex chaos with a bandwidth that outperforms QCL's chaos by more than one order of magnitude. A thorough analysis of the experimental time-series is carried out and confirms the hyperchaos nature of the nonlinear dynamics we generate. Our simulations based on the Lang-Kobayashi model are in good agreement with our experimental efforts and show that large bias currents are favorable for chaos generation.

[a)] Now at CREOL, College of Optics and Photonics, University of Central Florida, Orlando, Florida 32816, USA

[b)] Also at mirSense, Campus Eiffel, Bâtiment E-RDC, 1 rue Jean Rostand, Orsay, 91400, France

[c)] Also at Center for High Technology Materials, University of New-Mexico, 1313 Goddard SE, Albuquerque, New Mexico 87106, USA

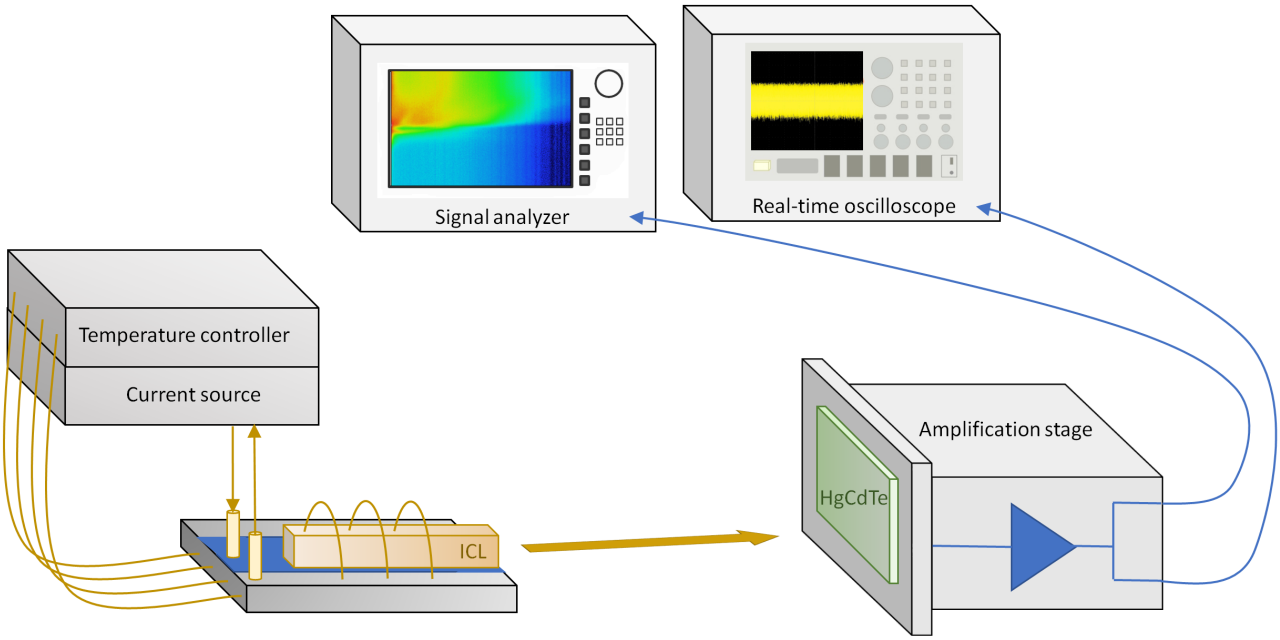

FIG. 1. Experimental setup for the generation and observation of nonlinear dynamics in an ICL. Analysis of the recorded time traces are performed either by a real-time oscilloscope or by a signal analyzer.

II. EXPERIMENTAL SETUP

Several methods were proven useful to generate nonlinear dynamics in semiconductor lasers. One can cite electro-optical feedback,[25,26] optical injection[27,28] and direct modulation.[29,30] Experiments with mid-infrared semiconductor lasers have focused on external optical feedback so far[31] and this is the configuration we implement in this article. The only difference is that in our previous efforts, external optical feedback was produced by a feedback mirror (or a tilted mirror to produce specific nonlinear dynamics[32]) with an external cavity of a few tens of centimeters while here, the laser can exhibit complex dynamics under solitary operation thanks to a combination of reflection close to the back-facet and potentially extra beating between many modes of the Fabry-Perot optical spectrum, even if we were not able to thoroughly confirm this claim, as explained in Appendix A.

The setup, described in Fig. 1, is made of a temperature-controlled laser that faces a fast Mercury-Cadmium-Telluride (HgCdTe) detector from Vigo Photonics, with a tabulated bandwidth of 0.8 GHz. This simplifies the experimental setup as an external cavity is not required but on the other hand, this means that we cannot tune the feedback strength. Consequently, the two levers to change the conditions of operation are temperature and bias current. The ICL under study is housed in a ILX LDM-4872 mount (this package can be visualized in Ref. 33) that allows accurate temperature control, and a focusing lens beside the front facet allows gathering the mid-infrared light so that it impinges on the active area of the HgCdTe detector. The electrical signal from the HgCdTe detector is sent to a signal analyzer (Rohde & Schwarz, FSW 50 GHz) that is operated in the spectrogram mode. The latter has a full-screen refresh time of 125 seconds when the analysis bandwidth is set to 2 GHz and for this reason, the ICL is modulated with a ramp signal at a frequency of 8 mHz, that is directly injected into the modulation input of our bias source (Wavelength Electronics, QCL2000). During this 125 seconds, the bias current of the ICL linearly varies from 75 mA to 180 mA and that allows plotting the frequency map in real time. For the mathematical characterization of chaos, one needs to record long time-series. In this case, the HgCdTe detector is connected to a real-time oscilloscope (Tektronix, MSO64) with a bandwidth of 2.5 GHz and a maximum sampling rate of 25 GS/s.

III. EXPERIMENTAL NONLINEAR DYNAMICS GENERATED BY THE ICL

Figure 2 shows the spectrograms of the signal retrieved when varying the laser bias current from 75 mA (just above threshold) to 180 mA (2.5 times threshold). At 15°C in Fig. 2 a), the ICL under study is stable for low bias current and starts to show destabilization above 110 mA. Then, up to the maximum bias current, the nonlinear dynamics have a broad spectrum that is limited by the bandwidth of the HgCdTe detector. The combination of broadest and flattest spectrum is found around 150 mA and this corresponds to the configuration that is highlighted in the RBG described in Appendix C. For this temperature of operation, it is difficult to clearly identify the relaxation frequency (f_R) that could correspond to the orange area spanning around 0.5-0.6 GHz between 150-180 mA. When increasing the temperature to 17.5°C in Fig. 2 b), the behavior is globally the same except that now, the relax-

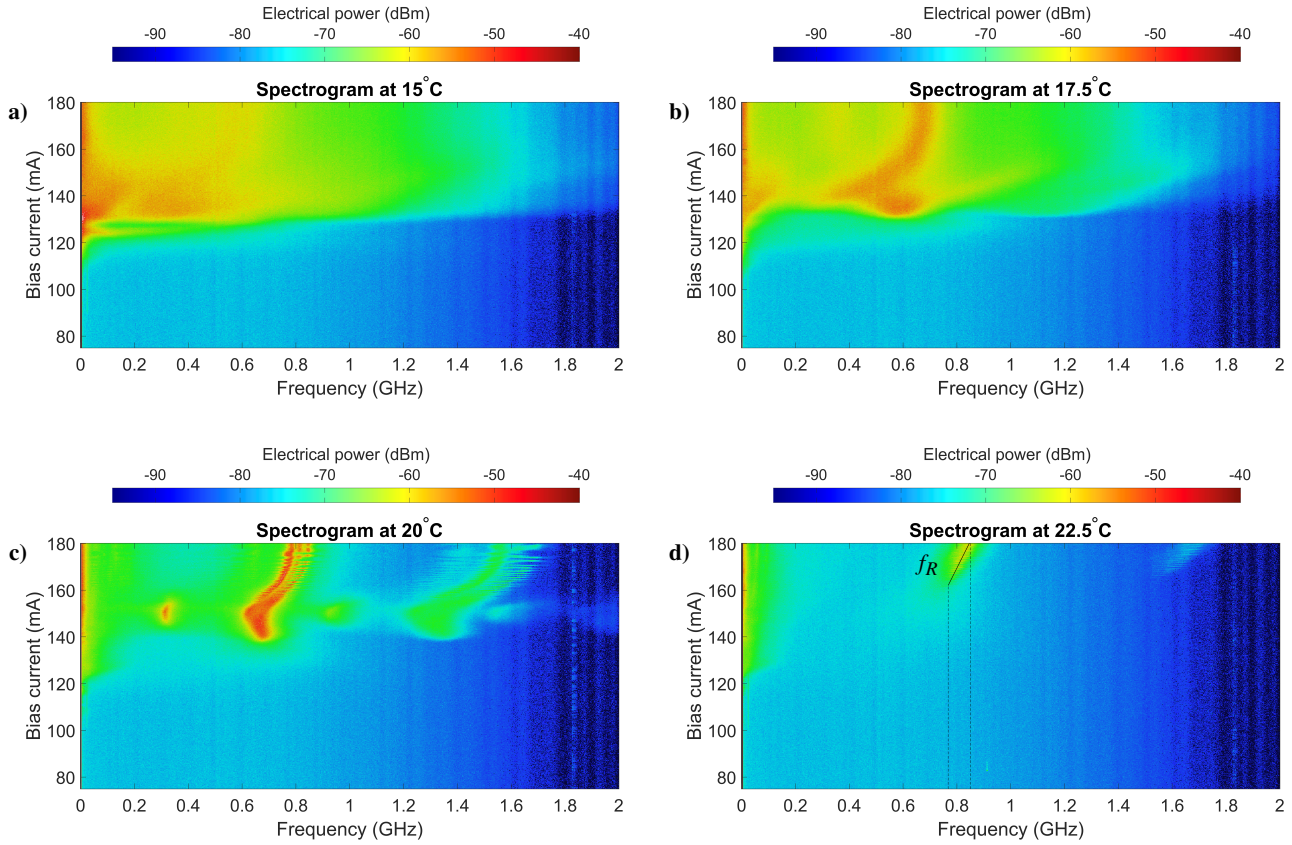

FIG. 2. Experimental spectrograms showing the evolution of the electrical spectrum when varying the bias current of the ICL for four temperatures a) 15°C; b) 17.5°C; c) 20°C; d) 22.5°C, in addition this spectrogram highlights the linear evolution of the relaxation frequency f_R (black solid line) for a bias current between 162-182 mA. For high frequencies, the signal is attenuated due to the limited bandwidth of the detector.

ation frequency can be clearly observed from 140 mA. This frequency increases with the bias current and that is compatible with our findings for another ICL optimized for high-frequency modulation.[7,34] It is relevant to note that in the latter references, we retrieved the relaxation oscillation with a relative intensity noise (RIN) technique and with a direct-modulation technique, respectively, which are different from the nonlinear dynamics analysis we are carrying out here. The conclusion is that three different methods give similar results for two ICLs with similar material characteristics. Overall, the low value of the relaxation oscillation frequency is attributed to the relatively long (3 mm) internal cavity of the lasers under study. Though the results at 17.5°C also show a broad electrical spectrum, this configuration is less interesting for applications like RBG or private communication because the relaxation frequency has a stronger influence than most of the frequencies, and this impacts the complexity of the signal. If one further increases the temperature to 20°C in Fig. 2 c), the electrical spectrum is no longer broad but mainly displays the evolution of the relaxation frequency with temperature, because this frequency is now the main component of the spectrum above 140 mA. Interestingly, the spectrogram shows a frequency doubling phenomenon for all the bias currents above 140 mA. As the detector has a limited bandwidth of 0.8 GHz, the intensity of frequencies in the 1.4-1.6 GHz range is attenuated and it is not possible to say if a higher multiple integer of the relaxation frequency is also excited. Recent progress in high-speed mid-infrared detectors now allows responsivities of several hundreds of mA/W at room temperature[35] and, in the future, we will have the opportunity to analyze how much what we observe in these spectrograms is limited by the bandwidth of our HgCdTe detector. At 20°C, it is also possible to see a period doubling phenomenon around 150 mA with four main frequency components: one around $\frac{1}{2} \times f_R$, one around f_R, another one around $\frac{3}{2} \times f_R$ and finally one around $2 \times f_R$. As one may notice, there is a discontinued pattern around f_R and around $2 \times f_R$ which locally broadens the frequency spectrum around these two values. Further investigation is required to explain this phenomenon. For the last temperature of our experimental study (22.5°C) in Fig. 2 d), the main frequency component that is observed is f_R and once again the dynamics complexity of the signal is reduced when increasing temperature. It is also possible to see the frequency doubling effect between 1.6-1.8 GHz, but the signal is very dim due to the frequency cut-off of the detector.

One can find in Appendix A details about various nonlinear dynamics that we observe with the aforementioned scheme.

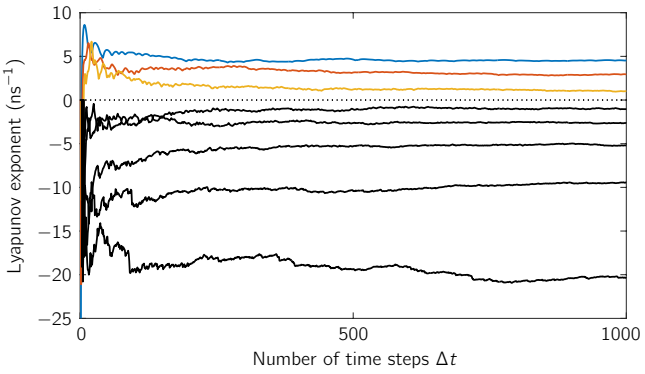

FIG. 3. Computation of the Lyapunov spectrum from an experimental time-series of the chaotic ICL with bias current I = 150 mA. The computation uses 80,000 samples with time-step $\Delta t = 40$ ps (the initial 1,000 iterations are shown in the figure to show the convergence). Considering an embedding dimension $d_E = 8$, only the corresponding Lyapunov exponents are represented here, the three positive Lyapunov exponents are in colored-lines.

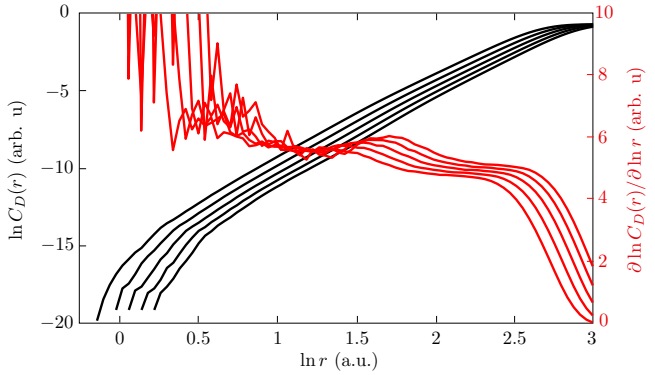

FIG. 4. Logarithm of the value of the correlation integral (black line) and slope of the logarithm of the value of the correlation integral (red line) as a function of an hyper-spherical radius r in the reconstructed phase-space. A plateau is found in the slope of the correlation integral. The estimated correlation dimension on the optical chaos is $D_c \approx 5.58$.

The most appropriate experimental set of data for chaos-based applications corresponds to the chaotic waveform and the electrical spectrum that were retrieved for a temperature of 15°C and a bias current of 150 mA. The advantage of this configuration is that the relaxation frequency is not seen (nor any other predominant frequency) and this improves the spectrum flatness. It is relevant to note that the chaos bandwidth shown in this article is much larger than that found in other experimental articles dealing with ICL chaos.[12,36]

IV. CHARACTERIZATION OF EXPERIMENTAL CHAOS

In this section, the objective is to provide a detailed analysis of the experimental chaotic time-series generated by the ICL. In order to go beyond the characterization given in Ref. 12 for another mid-infrared ICL subject to optical feedback, we complement the Lyapunov exponents computation by comparing the fractal dimension of the chaotic attractor with the information dimension extracted from the Lyapunov spectrum and by carrying out a statistical-based assessment of the nature of chaos.

A. Statistical detection of chaos

We use two advanced statistical-based methods to assess the presence of chaotic behavior: (i) the $0-1$ chaos test and (ii) the noise titration techniques.

On the one hand, we use a modified $0-1$ chaos test tailored for noisy experimental data and based on the so-called *chaos decision tree algorithm*.[37] The $0-1$ chaos test originally consists in generating two auxiliary variables from the intensity time-series and then, we estimate the growth rate K of the time-averaged mean-square displacement of the map. The value of K is indicative of the dynamical characteristics of the time-series: if $K = 1$ (respectively $K = 0$), the initial time-series is chaotic (respectively regular and non-chaotic).[38,39] In our analysis, we use 100,000 raw samples from the ICL intensity time-series and find that $K = 0.9984$. This value is within 0.0016 of $K = 1$ and consequently provides additional evidence to the presence of chaos in our experimental data.

On the other hand, we use the titration of chaos with additive noise.[40] This method has been used to demonstrate the presence of chaotic behavior in other experimental chaotic systems.[41,42] It performs a statistical test (Mann-Whitney test or F-test) to compare, with a significance level of 1%, the quality of one-step linear (auto-regressive) and nonlinear (Wiener-Volterra series) predictive models.[43] These comparisons are performed for decreasing signal-to-noise ratio (SNR) associated with the progressive addition of synthetic additive white Gaussian noise (AWGN) to the original data. We then call *Noise Limit* (*NL*) the noise threshold resulting in better accuracy of the linear predictive model compared to the nonlinear model. In the noise titration technique, $NL > 0$ is equivalent to detecting a strong nonlinear generation process in the time-series (*i.e.* chaos), whereas $NL = 0$ corresponds to the absence of nonlinearity or chaos. In our analysis, where we have considered a maximum degree $d = 2$ for the Wiener-Volterra series, a maximum memory depth $\kappa = 10$, and a subsampling factor of 20 (determined by the detection of a first minimum of the delayed mutual information), we find that $NL = 57\%$. This large value level for the Noise Limit provides, in addition to the $0-1$ test for chaos, additional evidence of the presence of ICL's deterministic chaos.

B. Lyapunov spectrum, Kaplan-Yorke dimension and Kolmogorov-Sinaï entropy

The nonlinear analysis of the intensity time-series is carried out through embedding techniques with a denoising filtering step that preserves all the relevant spectral features associated

with the dynamics.[44] The computation of the Lyapunov spectrum requires the use of a reconstructed phase space to characterize the expansion/contraction rate in each dimension. We determine the embedding dimension to be $d_E = 8$ based on false-nearest neighbor technique with a residual proportion of false neighbors $< 0.5\%$. Then, we consider the approach by Eckmann *et al.*[45] to compute the Lyapunov spectrum from the time-series considering 80,000 samples to get robust estimations. The convergence of the algorithm is illustrated in Fig. 3. We report hyperchaotic dynamics of the ICL under study, with three positive Lyapunov exponents at $\lambda_1 = 4.53 \pm 0.01$ ns^{-1}, $\lambda_2 = 2.80 \pm 0.02$ ns^{-1}, and $\lambda_3 = 0.84 \pm 0.03$ ns^{-1}. This further allows estimating the attactor's fractal dimension[46] using the Kaplan-Yorke conjecture: $D_{KY} = j + \sum_{i=1}^{j} \frac{\lambda_i}{|\lambda_{j+1}|} \approx 5.93$ with $j = 5$ such that $\sum_{i=1}^{j} \lambda_i > 0$ and $\sum_{i=1}^{j+1} \lambda_i \leq 0$. We obtain the Kolmogorov-Sinaï entropy[47] from the Pesin inequality,[48] which reads $h_{KS} = \sum_{i|\lambda_i>0} \lambda_i \approx 8.17$ ns^{-1}.

C. Correlation dimension analysis

The presence of chaos in experimental time-series is also linked to the fractal geometry of the physical system's attractor. To estimate the fractal dimension of the attractor, we implement the Grassberger-Procaccia (GP) algorithm.[49] It computes an estimation of the correlation dimension D_c using correlation summation that reads:

$$C_D(r) = \frac{2}{(N-n_T)(N-1-n_T)} \times \sum_{i=1}^{N} \sum_{j=i+1+n_T}^{N} \Theta\left(r - \|\mathbf{x}_i^{(d_e)} - \mathbf{x}_j^{(d_e)}\|\right) \quad (1)$$

where $\mathbf{x}_i^{(d_e)}$ is a d_e-dimensional vector constructed from the experimental time-series using a time-delay embedding, r is the radius of a d_e-dimension hyper-spherical neighborhood centered in $\mathbf{x}_i^{(d_e)}$, Θ is the Heaviside function and N is the number of vectors built from the experimental time-series. In addition, n_T is a threshold introduced by Theiler[50] satisfying the index inequality $|i-j| > n_T$ to prevent temporal correlation between vectors, which may induce spurious estimation of the correlation dimension. If the attractor is self-similar (*i.e.* fractal) then the correlation sum should theoretically exhibit a quasi-linear growth in log-scale, which translates into a constant slope (or plateau). The correlation dimension is then defined as follows:

$$D_c = \lim_{\substack{r\to 0 \\ N\to+\infty}} \frac{\partial \ln C_D(r)}{\partial \ln r} \quad (2)$$

To mitigate the effect of experimental noise in our estimation of D_c, we use a re-embedding procedure based on singular value analysis (SVA), which is an optimal linear transformation of the data to filter out the contribution of noise and to retain mostly the non-stochastic part of the system's dynamics in the GP algorithm. For the re-embedding, we consider a sliding time windows containing M samples from the initial time-series to convert it into a 2D data matrix of size $M \times (N-M+1)$. Finally, we perform a principal component analysis (PCA) and retain only the most significant principal components (PCs). As a result, the d_e- dimensional vectors $\mathbf{x}_i^{(m)}$ in the GP algorithm are substituted by vectors constructed from the retained PCs.[51]

We apply the GP algorithm combined with the re-embedding technique to the optical intensity time-series of the ICL. For the re-embedding, we sub-sample the time-series by a factor 2 and consider $N = 20{,}000$ samples. Then, we use a time-window of $40\Delta t = 1.6$ ns to create the aforementioned 2D data matrix. After performing the PCA, we keep the 7 most significant PCs for the GP algorithm and we also use a Theiler threshold of $n_T = 50$. The estimation of the correlation sum and its slope as a function of r are shown in Fig. 4 for increasing embedding dimensions $d_e = [12, 14, 16, 18, 20]$. We observe in the approximate range $1.0 < \ln r < 1.4$ a plateau in the slope: this value corresponds to an estimation of the correlation dimension $D_c = 5.58 \pm 0.11$. The estimation found here is of similar magnitude with that found using Lyapunov exponents and the Kaplan-Yorke conjecture. Furthermore, we have $D_c < D_{KY}$, which is consistent with the theory about the correlation dimension being strictly smaller than the information dimension estimated by the Kaplan-Yorke formula.[44]

V. MODELLING WITH LANG-KOBAYASHI MODEL

The nonlinear dynamics generated by an ICL subject to weak external optical feedback can be understood with the Lang-Kobayashi model on the basis of a rate equation approach.[52] This model is widely used in numerical simulations for diverse types of semiconductor lasers under self-feedback, such as quantum dot lasers[53] and quantum cascade lasers.[2] In the case of ICLs,[12] the modified rate equations of the number of carriers N, the number of photons S and the field's phase ϕ read:

$$\frac{dN(t)}{dt} = \eta \frac{I}{q} - \Gamma_p v_g g S(t) - \frac{N(t)}{\tau_{sp}} - \frac{N(t)}{\tau_{aug}} \quad (3)$$

$$\frac{dS(t)}{dt} = [m\Gamma_p v_g g - \frac{1}{\tau_p}]S(t) + m\beta \frac{N(t)}{\tau_{sp}} + 2\kappa\sqrt{S(t)S(t-\tau)}\cos\Delta(t) \quad (4)$$

$$\frac{d\phi(t)}{dt} = \frac{\alpha_H}{2}[m\Gamma_p v_g g - \frac{1}{\tau_p}] - \kappa\sqrt{\frac{S(t-\tau)}{S(t)}}\sin\Delta(t) \quad (5)$$

where I is the pump bias current, η is the laser injection efficiency, q is the elementary charge value, τ_{sp} is the spontaneous emission lifetime, τ_{aug} is the Auger recombination life-

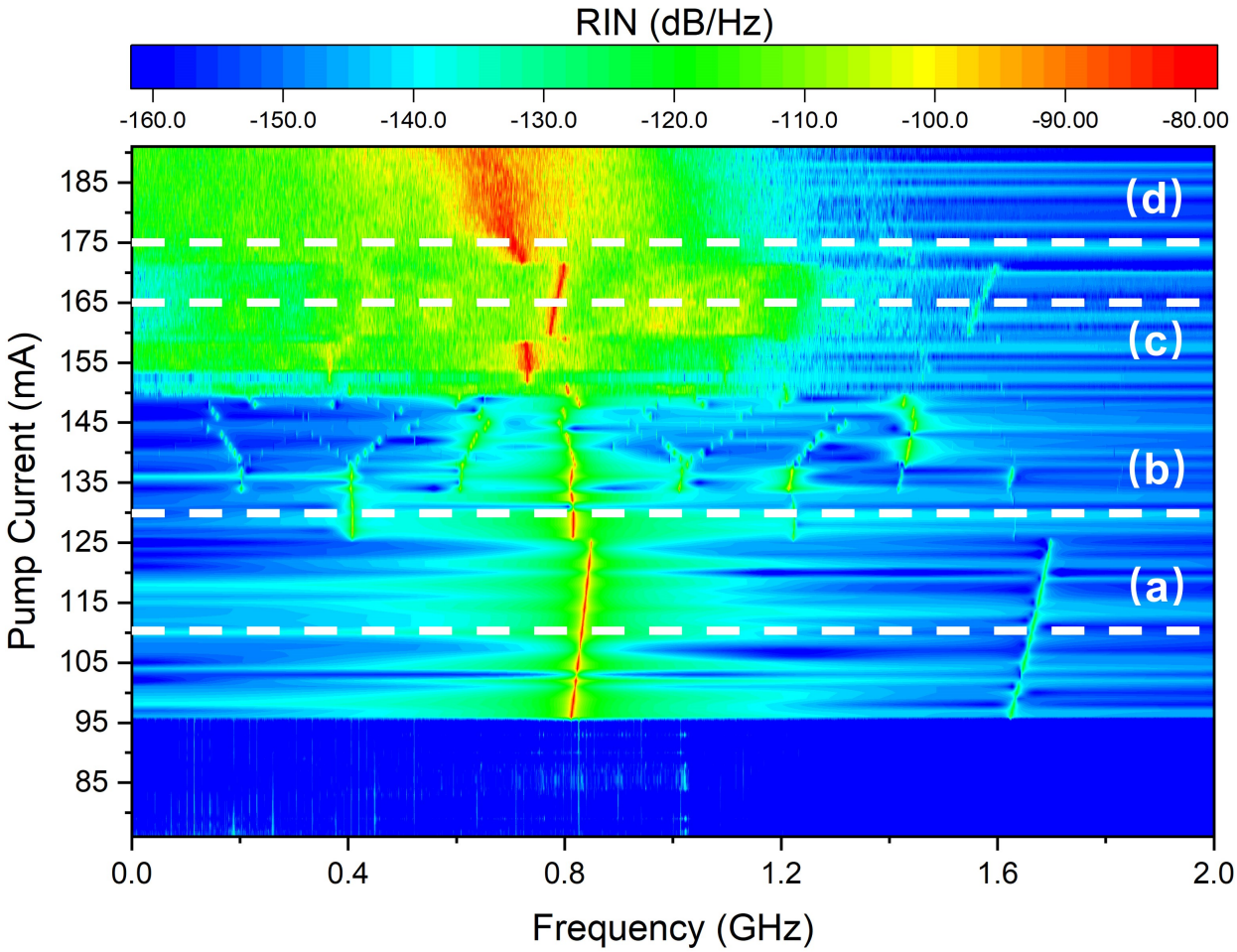

FIG. 5. Simulated spectrogram when varying the bias current of the ICL in a range similar to the experimental scheme. The horizontal dashed line corresponds to the four bias current conditions in Fig. 6.

time, Γ_p is the optical confinement factor, v_g is the group velocity of light expressed as $v_g = \frac{c}{n_r}$, m is the stage number, τ_p is the photon lifetime which is obtained from:[54]

$$\tau_p = \frac{1}{v_g[\alpha_{in} + \frac{1}{L}\ln\frac{1}{R}]} \tag{6}$$

β is the spontaneous emission factor, α_H is the linewidth enhancement factor, τ is the external-cavity delay time. g is the optical gain per stage which is defined as:

$$g = \frac{a_0[N(t) - N_0]}{A} \tag{7}$$

N_0 is the carrier number at transparency, a_0 is the differential gain coefficient and A is the area of the active region. $\Delta(t)$ is given by $\Delta(t) = \Psi_0 + \phi(t) - \phi(t-\tau)$ with Ψ_0 being the initial phase shift. Additionally, κ is the optical feedback term and can be written as:

$$\kappa = \frac{2C_l}{\tau_{in}}\sqrt{f_{ext}} \tag{8}$$

In Eq. 8, τ_{in} is the internal laser cavity round-trip time, and f_{ext} is the feedback strength that indicates the ratio between reflected light power and emitted output power. $C_l = \frac{1-R}{2\sqrt{R}}$ is the external coupling coefficient with R being the reflectivity of the laser facet facing the external mirror, whose expression is more complex in DFB lasers and depends on facet phases.[55] All the parameters values are listed in Table. I and the integration time step during the simulation is set as 0.5 ps. We integrate the delay differential rate equations Eqs. (3)-(5) numerically with the initial values given by the steady-state solution through the fourth-order Runge–Kutta algorithm. Importantly, the effect of noise is not included in our calculation since we want to distinguish between laser noise and deterministic chaos. The external cavity length is set to 4 cm in order to mimic the short-cavity feedback regime. It is relevant to point out that we set the feedback strength at a constant value (f_{ext} = 0.3%) to account for the experimental observa-

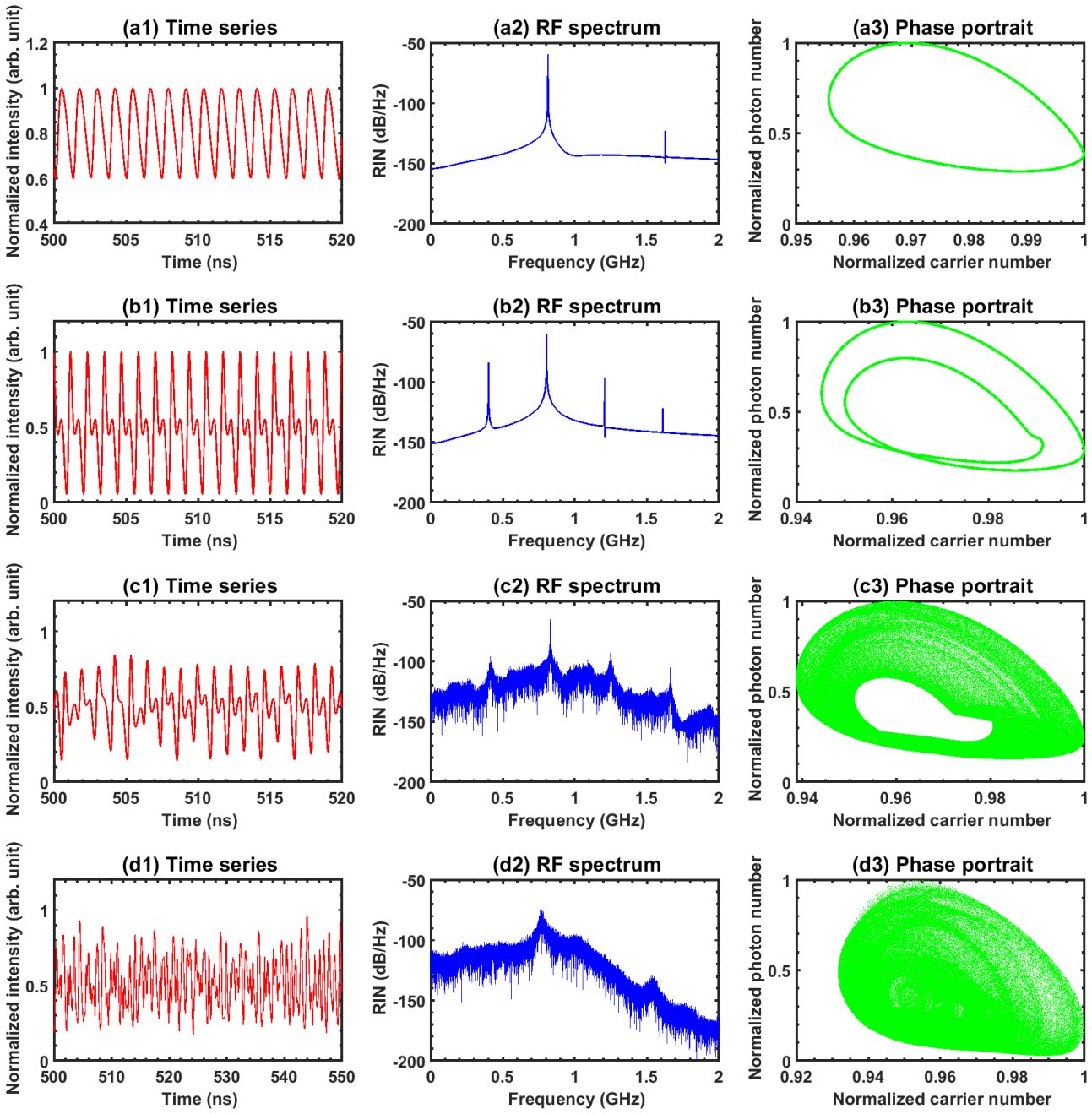

FIG. 6. Simulated characteristics of the dynamics for four bias currents compatible with the experimental scheme; a) 110 mA; b) 130 mA; c) 165 mA; d) 175 mA.

tion and we set the initial phase shift Ψ_0 as $1.2 \times \pi$ so as to obtain significant dynamics behaviors.

Based on the Lang and Kobayashi model, Fig. 5 depicts the simulated spectral evolution of the ICL under study as a function of the gradually increasing pump bias current. One can clearly observe that the laser experiences a typical period-doubling route to chaos[56] through Hopf bifurcations, leading to a strong line broadening for high bias current. For example, just above threshold, meaning 75 mA both in the experiments and in the simulations, the signal remains stable and there is no destabilization at all. Increasing the bias current up to around $1.5 \times I_{th}$ results in the appearance of two main frequency components, which are the relaxation frequency f_R and its first harmonic at $2 \times f_R$. Further increase of the current to $2 \times I_{th}$ allows displaying more discrete frequency peaks but, up to this current value, the dynamical behaviors are not chaos patterns. The bias value corresponding to the maximum experimental current $2.5 \times I_{th}$ gives rise to a much more complex electrical spectrum with strong relaxation frequency broadening followed by a dense area where remark-

able nonlinear dynamics can be found. It is relevant to note that, in these numerical simulations, a 0.8 GHz low-pass filter is applied in order to account for the limited bandwidth of the HgCdTe detector that is described in the experimental section. Experimentally, one can see that we had to tune the temperature between 15°C and 22.5°C to observe a variety of nonlinear phenomena. Numerically, such a small change in temperature has very limited effect on the simulation, but we are able to observe all the aforementioned nonlinear dynamics for a fixed value of temperature.

In order to give details about the dynamics that we are able to exhibit with the aforementioned simulation, we focus on four pump currents highlighted with white dashed lines in Fig. 5. In Fig. 6, the left column shows the calculated time-series and the center column shows the electrical power spectra obtained with Fourier transform. The time-series reveal that the ICL's output goes from stable operation at low bias current, then to periodic oscillation, and ultimately to an irregular signature at high bias current. The electrical power spectra confirm such oscillation at the relaxation frequency, as well as the period-doubling phenomenon. For instance, as seen in Fig. 6 row (b), one can observe the period-2 time-series and four main frequency components in the electrical spectrum that are located at $\frac{1}{2} \times f_R$, f_R, $\frac{3}{2} \times f_R$ and $2 \times f_R$, which agrees well with the experimental data displayed in Fig 2 c). However, this phenomenon is not of interest for applications because it corresponds to nonlinear dynamics with low complexity. For the maximum bias current, Fig. 6 row (d) displays chaos time-series and the electrical spectrum is broad. In addition, the right column exhibits the associated phase portraits with normalized carrier number and photon number. It is worth noting that limit cycle solutions and eventually chaotic attractors can be viewed from Fig. 6 (a3) to (d3). In summary, these numerical results are in good agreement with our experiments where relaxation oscillations and period-doubling phenomena have been observed. Also, it confirms that chaos can be observed at high bias currents, which have the advantage to give intense optical power and are compatible with applications.

TABLE I. Material and optical parameters of the ICL used in the simulation. Among all the parameters that are used in order to obtain the computational behavior we described, only η and α_H are not directly reproduced from other references. The values that are chosen for η and α_H are still in agreement with experimentally extracted parameters, see Refs. 7,57 and Refs. 58,59, respectively.

Symbol	Description	Value	Reference
L	Cavity length	3 mm	7
W	Cavity width	10 μm	7
R	Facet reflectivity	0.32	7
n_r	Refractive index	3.5	7
Γ_p	Optical confinement factor	0.23	7
α_{in}	Internal loss	5 cm^{-1}	7
m	Stage number	7	7
τ_{sp}	Spontaneous emission time	15 ns	7
τ_{aug}	Auger lifetime	1.08 ns	7
β	Spontaneous emission factor	10^{-4}	60
a_0	Differential gain	2.8×10^{-10} cm	61
N_0	Transparent carrier number	6.2×10^{7}	61
η	Current injection efficiency	0.15	Simulation driven
α_H	Linewidth enhancement factor	3.0	Simulation driven

VI. CONCLUSION

This work reported a broad and flat hyperchaos extending beyond 1 GHz at mid-infrared wavelength, and this was obtained with a solitary Fabry-Perot interband cascade laser. Mathematical analysis of the most relevant time-series for applications showed multiple proofs of the deterministic chaos nature of the nonlinear dynamics, with a *Noise Limit* of 57% and three positive Lyapunov exponents. Simulations with the Lang-Kobayashi model in the short-cavity regime confirmed that ICLs exhibit a period-doubling route to chaos, as well as deterministic chaos far from bias threshold. Overall, the numerical work is in good agreement with the experimental efforts. We believe this work opens up challenges for room-temperature mid-infrared applications based on high-speed ICLs and advocates for the development of sensitive fast detectors in this optical domain. Our analysis was indeed partially limited by our (yet very sensitive) HgCdTe detector whose frequency cut-off is below 1 GHz. In the near future, we expect that free-space communication and nonlinear pattern generation in the mid-infrared will greatly benefit from the next generation of detectors based on either frequency-conversion technology[62], unipolar quantum optoelectronics[63] or resonant cavities,[64] those already being able to operate at frequencies $\geq$ 5 GHz. In addition, upcoming efforts will study techniques to broaden the mid-infrared chaos bandwidth beyond the GHz range, for instance by implementing strong optical injection schemes[65] or by filtering and reinjecting residual optical side modes.[66]

ACKNOWLEDGMENTS

This work was supported by the French Defense Agency (DGA), the French ANR program under grant ANR-11-EQPX-0016 and the European Office of Aerospace Research and Development (FA8655-22-1-7032). This work was also supported in part by the Chair in Photonics. Authors thank Prof. Jean-Christophe Cousin for lending the signal analyzer used in this work for the experimental spectrogram analysis and also thank Prof. Benedikt Schwarz (TU Wien) for the opportunity to test a quantum cascade detector during the experiment. In addition, the authors gratefully acknowledge insightful exchanges with Kyungduk Kim and Prof. Hui Cao (Yale University) related to entropy-level calculations in time-series.

AUTHOR DECLARATIONS

The authors have no conflict to disclose.

DATA AVAILABILITY STATEMENT

The data that support the findings of this study are available from the corresponding author upon reasonable request.

Appendix A: Diversity of dynamics in the experimental data

In the following, we give details about four configurations corresponding to a given bias current of interest for each of the temperatures described previously. For a temperature of 15°C, we focus on a bias current of 150 mA because it gives the flattest chaos bandwidth and this peculiarity is of paramount importance for RBG (and more generally for applications based on optical chaos, such as LiDAR or private communication). Figure 7 shows the initial spectrogram at 15°C and the selected bias current of 150 mA, followed by the associated chaos timetrace and power spectrum. One can see that the waveform is complex, as already emphasized in the section about chaos characterization, and the bandwidth of this chaos pattern (which contains 80% of the total power in the electrical spectrum[26]) is 0.83 GHz and that is in good agreement with the tabulated bandwidth of the detector. In this application-oriented experiment, we tested a faster quantum cascade detector similar to the one described in Ref. 67, but the responsivity below 10 mA/W at 4.1 μm was detrimental for our analysis. With the HgCdTe detector, one can see that we have more than 20 dB of signal-to-noise-ratio for frequencies up to 1 GHz (transition between the green/yellow area and the blue/cyan area in the spectrogram), and this allows extracting time series that require very few noise-filtering.

When increasing the temperature to 17.5°C, it is no longer possible to exhibit areas where the chaos spectrum is flat. In that case, we focus on a bias current of 133 mA, as shown in Fig. 8. Even if the spectrogram does not seem very different, this has a tremendous impact on the timetrace and one can clearly see in Fig. 8 b) that the signal is now much less complex, with a predominant high frequency modulated by a lower frequency. These characteristics are clearly observed in the electrical spectrum (Fig. 8 c)) and the dynamics we exhibit here is not relevant for most of the aforementioned applications.

A temperature of 20°C allows exhibiting a typical period doubling phenomenon when the bias current is 148 mA. As can be observed in Fig. 9, multiple harmonics of the half-frequency of relaxation are clearly displayed in the spectrum. The related timetrace shows a dual period corresponding to the two most predominant frequencies of the system (red areas around 0.31 GHz and 0.62 GHz). As for the previous case, this nonlinear phenomenon is not categorized as broadband chaos and is of little interest for applications. It is also relevant to note that the limited bandwidth of the HgCdTe detector hinders the analysis of higher harmonics that could exist above 2 GHz but are not seen with our current setup.

For the maximum 22.5°C temperature we investigated, the only phenomenon that is observed for high bias current is oscillation at the relaxation frequency, with a frequency-doubling pattern that is strongly attenuated by the limited bandwidth of our detector, as shown in Fig. 10. In good agreement with our previous work,[7] this configuration with a higher temperature gives a faster relaxation frequency. Generation of high-speed sine wave can be of interest for photonics-assisted radio-frequency transmissions but feedback dynamics, like the ones we just described, are generally limited by the external cavity frequency or by the relaxation frequency of the structure and do not allow accessing relevant communication bands, such as the W-band between 75-110 GHz. Other methods, such as optical injection[68] and heterodyne beating,[69] offer alternatives for all-optical millimeter-wave generation.

Due to the absence of true external cavity, one of the hypotheses to explain the diversity of dynamics that we observe is the interaction between several Fabry-Perot modes. Recent efforts showed that it is even possible to tune the multimode emission of a microcavity laser[70,71] in order to tailor the chaos bandwidth of this laser. In our case, one can find the optical spectra of the ICL in Fig. 11. Those were obtained at a temperature of 15°C in a configuration where the ICL was not chaotic (Fig. 11 a)) and in another configuration where the ICL exhibited broadband chaos (Fig. 11 b)). The two spectra show multimode emission, but the number of modes increases with the bias current and, as expected, there is a redshift of the central wavelength when increasing bias current. Yet, it is not really possible to extract any mode interaction that would enhance the mid-infrared chaos bandwidth and this is due to the resolution of our Fourier Transform Infrared Spectrometer (FTIR, Nicollet iS50) that is limited to 25 pm (or equivalently, 0.43 GHz at 4.18 μm). Finally, the optical spectrum in Fig. 11 b) allows deriving an average intermode frequency of 13 GHz, which gives a cavity length of 3.3 mm if we consider a refractive index of 3.5. This cavity length value is within 10% of the expected cavity length of 3 mm.

Appendix B: Entropic limit for randomness extraction

The capacity for physical entropy sources, such as chaotic ICLs, to generate random numbers at high-speed is bounded by the Shannon-Hartley limit[72] that reads, $h_{SH} = 2B_W N_\varepsilon$ with B_W the total bandwidth including the device and the measurement apparatus, and N_ε the number of quantification bits for a bin size ε. This upper limit is obtained under the provision of uniformly distributed samples and acquisition rate at the Shannon-Nyquist limit. However, with physical devices, those are generally not satisfied and the maximum entropy rate is then given by the more general expression (see Ref. 73 for more details):

$$h_{SH} = \min\left(1/T_s, 2B_W\right)\left[N_\varepsilon + D_{KL}(p(x)||u(x))\right], \qquad \text{(B1)}$$

with $1/T_s$ the sampling frequency of the measurement device, and $D_{KL}(p(x)||u(x))$ the Kullback-Leibler (KL) distance between $p(x)$ the estimated probability distribution of the experimental data and $u(x)$ the uniform distribution taken over the maximal range of the recorded data and defined as:

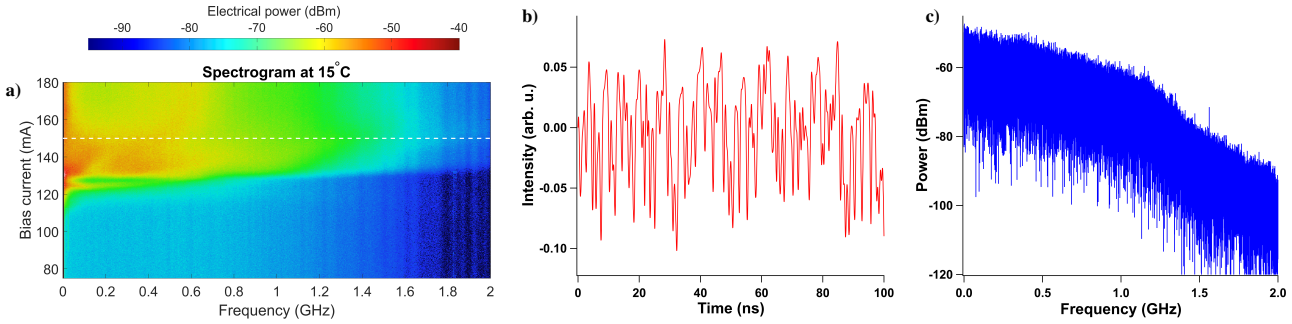

FIG. 7. Experimental characteristics of the optical chaos that is subsequently used for RBG; a) spectrogram at 15°C with a dashed white line highlighting the bias current of interest (150 mA); b) temporal timetrace showing the complex non-linear dynamics; c) electrical spectrum showing a flat behavior with the bandwidth of the detector (0.8 GHz) limiting the analysis.

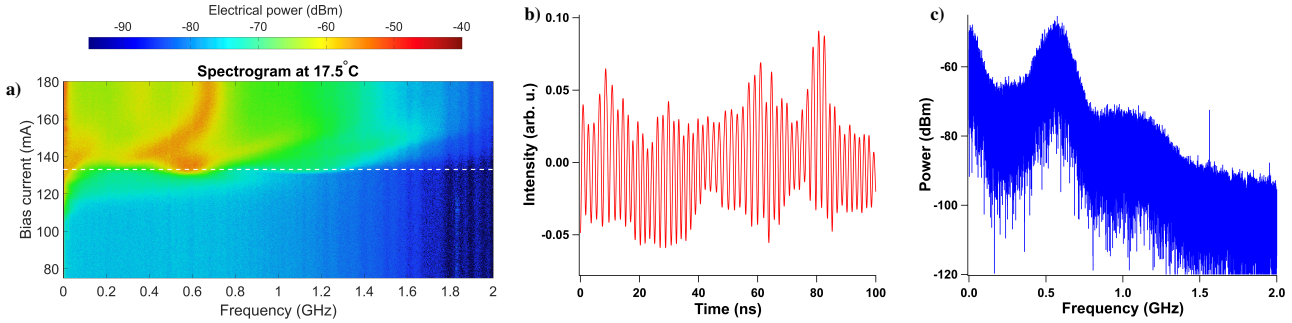

FIG. 8. Experimental characteristics of non-linear dynamics strongly driven by the relaxation frequency; a) spectrogram at 17.5°C with a dashed white line corresponding to 133 mA; b) temporal timetrace showing the non-linear dynamics; c) electrical spectrum.

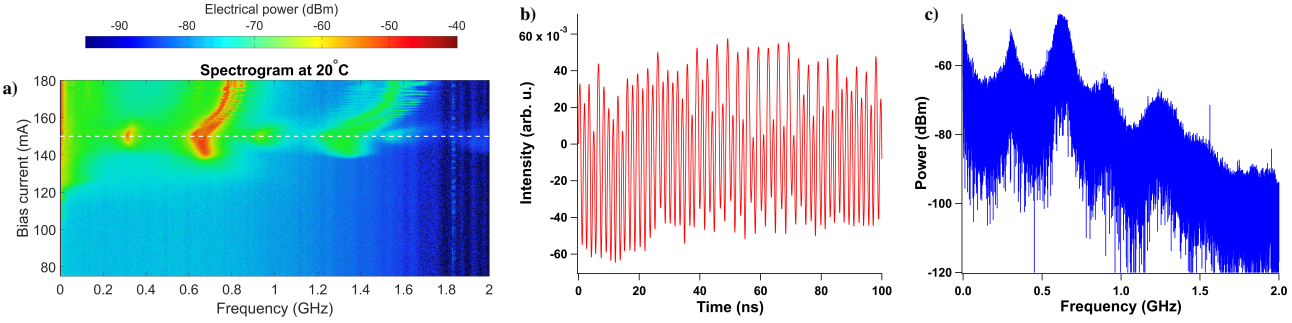

FIG. 9. Experimental characteristics of period-doubling dynamics; a) spectrogram at 20°C with a dashed white line corresponding to 148 mA; b) temporal timetrace showing the period-doubling dynamics; c) electrical spectrum showing four main frequency contributions.

$$D_{KL}(p(x)||u(x)) = \int p(x)\log_2(\frac{p(x)}{u(x)})dx \qquad \text{(B2)}$$

Considering the experimental time-series with well-developed chaos for pumping current I = 150 mA, we estimate the distribution $p(x)$ by computing the histogram of the time-series and numerically estimate $D_{KL} \approx -0.425$. As a result, the maximum extractable entropy rate from the chaotic ICL is $h_{SH} \approx 30.3$ Gbps.

Appendix C: Physical random bit generation

In this section, we show that ICLs' hyperchaos can be of interest for applications and we experimentally demonstrate a fast RBG at 25 Gbps based on the temporal chaos that we described previously. As detailed in the previous section, the limited bandwidth of the detector led to a corrected Shannon-Hartley limit of roughly 30 Gbps that will eventually be the maximum data rate for random bit generation with our configuration. In recent years, various groups have implemented RBG processes in a wide range of optical systems from random fiber lasers[74,75] to optomechanical

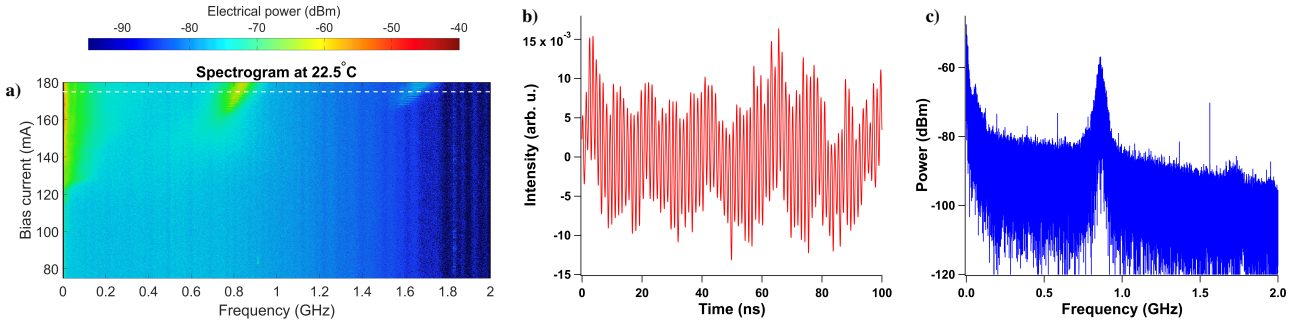

FIG. 10. Experimental characteristics of non-linear dynamics with relaxation oscillations and a small frequency-doubling contribution (attenuated by the limited bandwidth of the detector); a) spectrogram at 22.5°C with a dashed white line corresponding to 175 mA; b) temporal timetrace showing the non-linear dynamics; c) electrical spectrum.

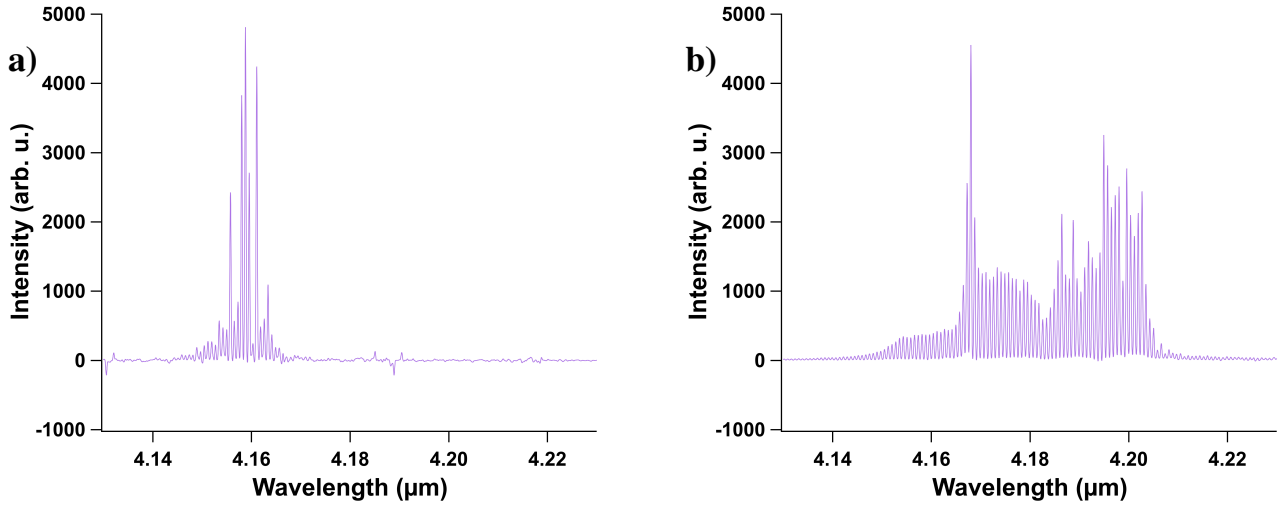

FIG. 11. Optical spectrum of the ICL under study when the temperature is 15°C a) for a bias current of 85 mA, corresponding to a case without temporal dynamics; b) for a bias current of 150 mA corresponding to a case with well-developed temporal chaos dynamics.

microcavities,[76] and overall, the topic of complex dynamics for RBG remains vivid.[77–82] The proposed post-processing scheme combines a high-order derivative algorithm[83] and a bit-order reversal bitwise exclusive-or (XOR) post-processing operation, adapted from the approach by Akizawa *et al.* with 8-bit vertical resolution.[84] The schematic of our RBG method is illustrated in Fig. 12. In the high-order derivative algorithm part, the chaotic signal was initially converted to an electronic signal by the HgCdTe detector, and multiple alterable-delay digitized signals were used to obtain the n^{th} discrete derivative.

The bit-order reversal procedure is shown in Fig. 13. After the 7^{th} derivative is calculated, the result is divided into two signals, one of which is 34.055 μs time-delayed to avoid cross-correlation between the two signals. The two electronic signals are simultaneously sampled at a fixed clock rate with

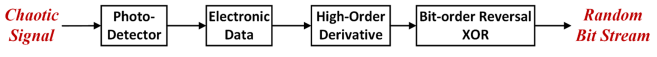

FIG. 12. Schematic diagram of the processes implemented in order to produce random bits with the experimental hyperchaos generated by the solitary ICL.

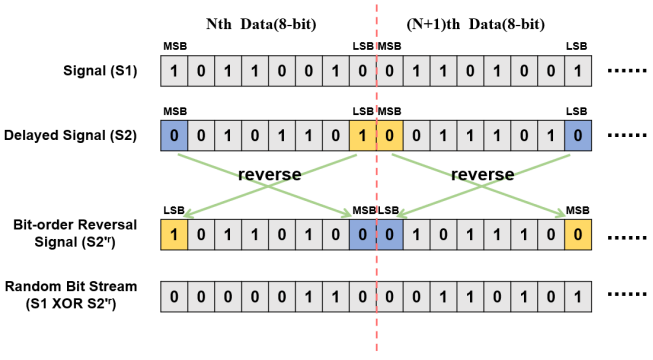

FIG. 13. Details of the bit-reversal XOR operation between signal S1 and delayed signal S2, which consists of swapping the least significant bit (LSB) and the most significant bit (MSB).

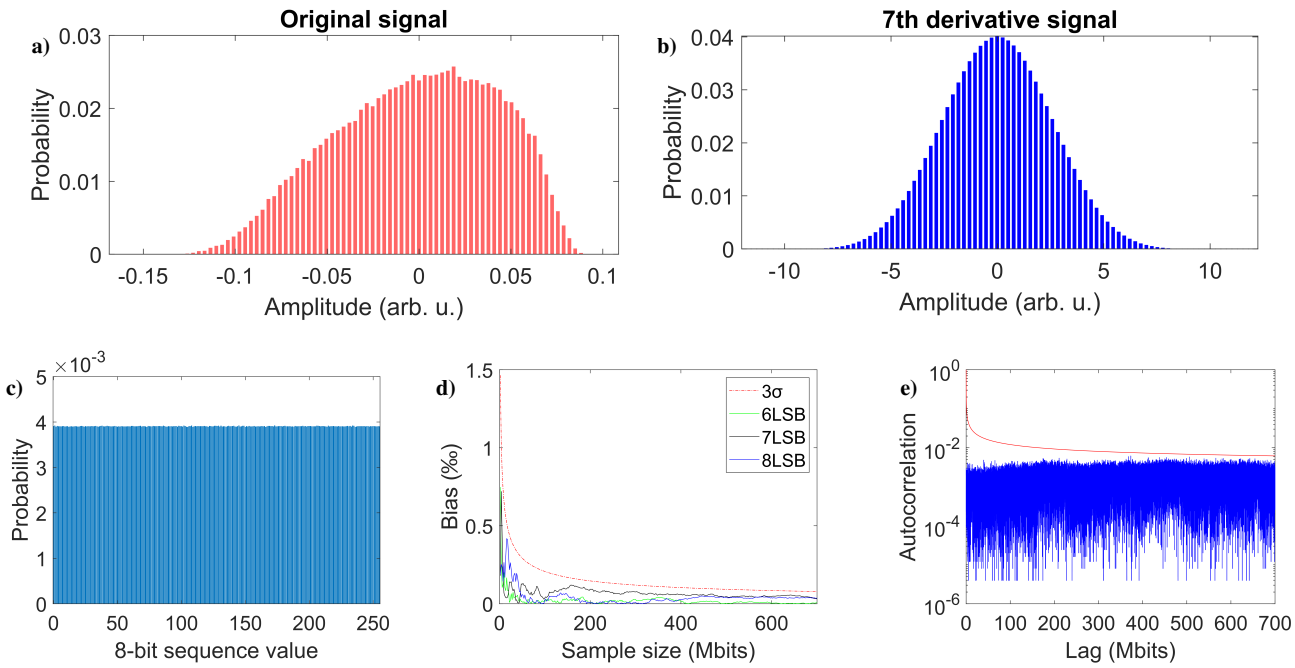

FIG. 14. Characterization of the signal used for random bit generation. a) distribution of amplitude for the original chaotic signal downsampled to a sampling rate of 3.125 GS/s; b) distribution of amplitude for the 7^{th}-derivative post-processed 3.125 GS/s timetrace; c) probability distribution of the 8-bit sequence value obtained after post-processing of the 7^{th}-derivative timetrace; d) statistical bias of random sequence with 6,7,8-LSB processes and comparison with the 3-σ limit; e) autocorrelation coefficient denoted 8-LSB bit sequence.

8-bit resolution to obtain two 8-bit sequences: signal S1 and delayed signal S2, respectively. Then the order of every 8-bit data stream of S2 is reversed for each sampling data, i.e. the 8-bit data $a_8a_7...a_1$ are converted to $a_1...a_7a_8$, with a_i the i^{th} significant bits. The bit-order-reversed 8-bit S2 signal is called $S2^{'r}$, thus the most significant bit (MSB) turns to least significant bit (LSB) and the least significant bit turns to most significant bit. Eventually, XOR operation is performed between every 8-bit data of signal S1 and signal $S2^{'r}$ so that we could obtain the random bit sequence.

It is relevant to note that, with this method, no bit is eliminated, and this differs from previous methods like extracting LSBs.[76] All of the 8 bits can be used for RBG which can effectively increase generation rate. Figure 14 a) shows the distribution of the original electronic signal that is downsampled from 25 GS/s to 3.125 GS/s, while Fig. 14 b) shows the distribution of the 7^{th}-derivative result, the latter indicating that the derivative method can achieve gaussian-like distribution. Fig-

TABLE II. Results of NIST tests.

NIST test	p-value	Proportion	Result
Frequency	0.550347	0.984	Success
Block-frequency	0.534146	0.988	Success
Cumulative-sums	0.397688	0.984	Success
Runs	0.715679	0.981	Success
Longest-run	0.344048	0.988	Success
Rank	0.063615	0.992	Success
FFT	0.195864	0.988	Success
Non overlapping-template	0.649612	0.992	Success
Overlapping-template	0.858002	0.984	Success
Universal	0.357000	0.996	Success
Approximate entropy	0.574903	0.981	Success
Random-excursions	0.722135	0.989	Success
Random-excursions-variant	0.698104	0.994	Success
Serial	0.494392	0.984	Success
Linear-complexity	0.363593	0.988	Success

TABLE III. Result of Diehard tests.

Diehard test	p-value	Assessment
Birthday spacing	0.86944941	Passed
Overlapping 5-permutation	0.18288592	Passed
Binary rank for 32 × 32 matrices	0.51547518	Passed
Binary rank for 6 × 8 matrices	0.90019978	Passed
Bitstream	0.23850040	Passed
Overlapping-Paris-Sparce-occupancy	0.22296190	Passed
Overlapping-Quadruples-Sparce-occupancy	0.57949254	Passed
DNA	0.37955114	Passed
Count-the-1's in a stream of bytes	0.52427260	Passed
Count-the-1's for specific bytes	0.86043748	Passed
Parking lot	0.59516268	Passed
Minimum distance	0.28734451	Passed
3D spheres	0.97551664	Passed
Squeeze	0.26074910	Passed
Sums	0.06853903	Passed
Runs	0.06857172	Passed
Craps	0.49872490	Passed

ure 14 c) is the probability distribution histogram in the case of 8-bit sequences, demonstrating equiprobability for the 256 possible values. As shown in Fig. 14 d), we tested the statistical bias of the retained 6, 7 and 8-LSB sequences. The statistical bias B is defined as: $B = P_1 - 0.5$, where P_1 is the probability of '1' in the bit sequence. The bias level is considered compatible if it is lower than the 3-sigma criterion[85] ($3\sigma = \frac{3}{2\sqrt{N_b}}$ where N_b is the number of random bits). As one can see, whatever the number of retained LSB, the bias is under the 3-sigma threshold, which means that we can achieve the maximum 8 $\times$ 3.125 GS/s = 25 Gbps rate for RBG and this value complies with the aforementioned Shannon-Hartley limit. Finally, Fig. 14 e) gives the autocorrelation of the bit sequence with 8-LSB, and the value of this coefficient is lower than the standard 3-sigma criterion. We tested the generated bit sequences with both NIST tests (Table II) and Diehard tests (Table III). Every single test shows valid p-value and qualified randomness. The NIST tests were used to evaluate the statistical randomness of the experimental bit sequences.[86] For NIST test's 'success', the p-value should be larger than 0.0001 and the pass proportion should be within $1-\alpha_{SL} \pm 3\sqrt{\frac{\alpha_{SL}(1-\alpha_{SL})}{N_{seq}}}$, i. e. in the range of 0.99 ± 0.0094392 using a number N_{seq} of 1000 sequences of one million bit data with a significance level of $\alpha_{SL} = 0.01$.[24] For the tests that produce multiple p-values and proportions, the worst case is given. In addition, the Diehard tests are a battery of statistical tests for measuring the quality of a random number generator, including twelve tests for which the process is repeated with different parameters.[87]

[1] O. Spitz and F. Grillot, "A review of recent results of mid-infrared quantum cascade photonic devices operating under external optical control," Journal of Physics: Photonics **4**, 022001 (2022).

[2] L. Jumpertz, K. Schires, M. Carras, M. Sciamanna, and F. Grillot, "Chaotic light at mid-infrared wavelength," Light: Science & Applications **5**, e16088–e16088 (2016).

[3] O. Spitz, A. Herdt, J. Wu, G. Maisons, M. Carras, C.-W. Wong, W. Elsäßer, and F. Grillot, "Private communication with quantum cascade laser photonic chaos," Nature communications **12**, 1–8 (2021).

[4] O. Spitz, J. Wu, M. Carras, C.-W. Wong, and F. Grillot, "Low-frequency fluctuations of a mid-infrared quantum cascade laser operating at cryogenic temperatures," Laser Physics Letters **15**, 116201 (2018).

[5] X.-G. Wang, B.-B. Zhao, Y. Deng, V. Kovanis, and C. Wang, "Nonlinear dynamics of a quantum cascade laser with tilted optical feedback," Physical Review A **103**, 023528 (2021).

[6] H. Han, X. Cheng, Z. Jia, and K. A. Shore, "Nonlinear dynamics of interband cascade laser subjected to optical feedback," in *Photonics*, Vol. 8 (Multidisciplinary Digital Publishing Institute, 2021) p. 366.

[7] P. Didier, O. Spitz, L. Cerutti, D. Diaz-Thomas, A. Baranov, M. Carras, and F. Grillot, "Relative intensity noise and intrinsic properties of RF mounted interband cascade laser," Applied Physics Letters **119**, 171107 (2021).

[8] J. Northern, S. O'Hagan, B. Fletcher, B. Gras, P. Ewart, C. Kim, M. Kim, C. Merritt, W. Bewley, C. Canedy, *et al.*, "Mid-infrared multi-mode absorption spectroscopy using interband cascade lasers for multi-species sensing," Optics letters **40**, 4186–4189 (2015).

[9] C. R. Webster, P. R. Mahaffy, S. K. Atreya, J. E. Moores, G. J. Flesch, C. Malespin, C. P. McKay, G. Martinez, C. L. Smith, J. Martin-Torres, *et al.*, "Background levels of methane in Mars' atmosphere show strong seasonal variations," Science **360**, 1093–1096 (2018).

[10] S. Zhao and F. Grillot, "Modeling of Amplitude Squeezing in a Pump-Noise-Suppressed Interband Cascade Laser," IEEE Photonics Journal **14**, 1–8 (2022).

[11] S. Zhao and F. Grillot, "Stochastic Model of Sub-Poissonian Quantum Light in an Interband Cascade Laser," Physical Review Applied **18**, 064027 (2022).

[12] Y. Deng, Z.-F. Fan, B.-B. Zhao, X.-G. Wang, S. Zhao, J. Wu, F. Grillot, and C. Wang, "Mid-infrared hyperchaos of interband cascade lasers," Light: Science & Applications **11**, 1–10 (2022).

[13] V. Ahlers, U. Parlitz, and W. Lauterborn, "Hyperchaotic dynamics and synchronization of external-cavity semiconductor lasers," Physical Review E **58**, 7208 (1998).

[14] H.-L. Ho, J.-D. Chen, C.-A. Yang, C.-C. Liu, C.-T. Lee, Y.-H. Lai, and F.-Y. Lin, "High-speed 3D imaging using a chaos lidar system," The European Physical Journal Special Topics , 1–7 (2022).

[15] J.-D. Chen, H.-L. Ho, H.-L. Tsay, Y.-L. Lee, C.-A. Yang, K.-W. Wu, J.-L. Sun, D.-J. Tsai, and F.-Y. Lin, "3D chaos lidar system with a pulsed master oscillator power amplifier scheme," Optics Express **29**, 27871–27881 (2021).

[16] A. Uchida, K. Amano, M. Inoue, K. Hirano, S. Naito, H. Someya, I. Oowada, T. Kurashige, M. Shiki, S. Yoshimori, *et al.*, "Fast physical random bit generation with chaotic semiconductor lasers," Nature Photonics **2**, 728–732 (2008).

[17] I. Reidler, Y. Aviad, M. Rosenbluh, and I. Kanter, "Ultrahigh-speed random number generation based on a chaotic semiconductor laser," Physical review letters **103**, 024102 (2009).

[18] T. Harayama, S. Sunada, K. Yoshimura, P. Davis, K. Tsuzuki, and A. Uchida, "Fast nondeterministic random-bit generation using on-chip chaos lasers," Physical Review A **83**, 031803 (2011).

[19] J. Wu, X. Tang, Z. Wu, G. Xia, and G. Feng, "Parallel generation of 10 Gbits/s physical random number streams using chaotic semiconductor lasers," Laser Physics **22**, 1476–1480 (2012).

[20] N. Oliver, M. C. Soriano, D. W. Sukow, and I. Fischer, "Fast random bit generation using a chaotic laser: approaching the information theoretic limit," IEEE Journal of Quantum Electronics **49**, 910–918 (2013).

[21] N. Li, B. Kim, V. Chizhevsky, A. Locquet, M. Bloch, D. Citrin, and W. Pan, "Two approaches for ultrafast random bit generation based on the chaotic dynamics of a semiconductor laser," Optics express **22**, 6634–6646 (2014).

[22] R. Sakuraba, K. Iwakawa, K. Kanno, and A. Uchida, "Tb/s physical random bit generation with bandwidth-enhanced chaos in three-cascaded semiconductor lasers," Optics express **23**, 1470–1490 (2015).

[23] X. Tang, Z.-M. Wu, J.-G. Wu, T. Deng, J.-J. Chen, L. Fan, Z.-Q. Zhong, and G.-Q. Xia, "Tbits/s physical random bit generation based on mutually coupled semiconductor laser chaotic entropy source," Optics Express **23**, 33130–33141 (2015).

[24] K. Kim, S. Bittner, Y. Zeng, S. Guazzotti, O. Hess, Q. J. Wang, and H. Cao, "Massively parallel ultrafast random bit generation with a chip-scale laser," Science **371**, 948–952 (2021).

[25] L. Larger, J.-P. Goedgebuer, and F. Delorme, "Optical encryption system using hyperchaos generated by an optoelectronic wavelength oscillator," Physical review E **57**, 6618 (1998).

[26] F. Lin and J. Liu, "Nonlinear dynamical characteristics of an optically injected semiconductor laser subject to optoelectronic feedback," Optics Communications **221**, 173–180 (2003).

[27] T. Simpson, J. Liu, A. Gavrielides, V. Kovanis, and P. Alsing, "Period-doubling route to chaos in a semiconductor laser subject to optical injection," Applied Physics Letters **64**, 3539–3541 (1994).

[28] T. Simpson, J. Liu, K.-F. Huang, and K. Tai, "Nonlinear dynamics induced by external optical injection in semiconductor lasers," Quantum and Semiclassical Optics: Journal of the European Optical Society Part B **9**, 765 (1997).

[29] H. Winful, Y. Chen, and J. Liu, "Frequency locking, quasiperiodicity, and chaos in modulated self-pulsing semiconductor lasers," Applied physics letters **48**, 616–618 (1986).

[30] G. P. Agrawal, "Effect of gain nonlinearities on period doubling and chaos in directly modulated semiconductor lasers," Applied physics letters **49**, 1013–1015 (1986).

[31] L. Jumpertz, M. Carras, K. Schires, and F. Grillot, "Regimes of external optical feedback in 5.6 μ m distributed feedback mid-infrared quantum cascade lasers," Applied Physics Letters **105**, 131112 (2014).

[32] O. Spitz, J. Wu, A. Herdt, G. Maisons, M. Carras, W. E. Elsäßer, C.-W. Wong, and F. Grillot, "Extreme events in quantum cascade lasers," Advanced Photonics **2**, 066001 (2020).

[33] O. Spitz, A. Herdt, W. Elsässer, and F. Grillot, "Stimulating polarization switching dynamics in mid-infrared quantum cascade lasers," JOSA B **38**, B35–B39 (2021).

[34]P. Didier, H. Knötig, O. Spitz, L. Cerutti, A. Lardschneider, E. Awwad, D. Diaz-Thomas, A. Baranov, R. Weih, J. Koeth, *et al.*, "Interband cascade technology for energy-efficient mid-infrared free-space communication," Photonics Research **11**, 582–590 (2023).
[35]Z. Shen, J. Yao, J. Huang, Z. Dai, L. Wang, F. Liu, X. Zou, B. Peng, W. Liu, H. Lu, *et al.*, "High-Speed Mid-Wave Infrared Uni-Traveling Carrier Photodetector with Inductive Peaked Dewar Packaging," Journal of Lightwave Technology (2023).
[36]M. Zhao, G. Xia, K. Yang, S. Liu, J. Liu, Q. Wang, J. Liu, and Z. Wu, "Nonlinear Dynamics of Mid-Infrared Interband Cascade Lasers Subject to Variable-Aperture Optical Feedback," in *Photonics*, Vol. 9 (MDPI, 2022) p. 410.
[37]D. Toker, F. T. Sommer, and M. D'Esposito, "A simple method for detecting chaos in nature," Communications biology **3**, 11 (2020).
[38]G. A. Gottwald and I. Melbourne, "Testing for chaos in deterministic systems with noise," Physica D: Nonlinear Phenomena **212**, 100–110 (2005).
[39]G. A. Gottwald and I. Melbourne, "On the implementation of the 0–1 test for chaos," SIAM Journal on Applied Dynamical Systems **8**, 129–145 (2009).
[40]C.-S. Poon and M. Barahona, "Titration of chaos with added noise," Proceedings of the national academy of sciences **98**, 7107–7112 (2001).
[41]S. Hu and A. Raman, "Chaos in atomic force microscopy," Physical Review Letters **96**, 036107 (2006).
[42]T. Devolder, D. Rontani, S. Petit-Watelot, K. Bouzehouane, S. Andrieu, J. Létang, M.-W. Yoo, J.-P. Adam, C. Chappert, S. Girod, *et al.*, "Chaos in magnetic nanocontact vortex oscillators," Physical review letters **123**, 147701 (2019).
[43]M. Barahona and C.-S. Poon, "Detection of nonlinear dynamics in short, noisy time series," Nature **381**, 215–217 (1996).
[44]H. Kantz and T. Schreiber, *Nonlinear time series analysis*, Vol. 7 (Cambridge university press, 2004).
[45]J.-P. Eckmann, S. O. Kamphorst, D. Ruelle, and S. Ciliberto, "Liapunov exponents from time series," Physical Review A **34**, 4971 (1986).
[46]J. L. Kaplan and J. A. Yorke, "Chaotic behavior of multidimensional difference equations," in *Functional differential equations and approximation of fixed points* (Springer, 1979) pp. 204–227.
[47]P. Grassberger and I. Procaccia, "Estimation of the Kolmogorov entropy from a chaotic signal," Physical review A **28**, 2591 (1983).
[48]Y. B. Pesin, "Characteristic Lyapunov exponents and smooth ergodic theory," Russian Mathematical Surveys **32**, 55 (1977).
[49]P. Grassberger and I. Procaccia, "Characterization of strange attractors," Physical review letters **50**, 346 (1983).
[50]J. Theiler, "Spurious dimension from correlation algorithms applied to limited time-series data," Physical review A **34**, 2427 (1986).
[51]K. Fraedrich and R. Wang, "Estimating the correlation dimension of an attractor from noisy and small datasets based on re-embedding," Physica D: Nonlinear Phenomena **65**, 373–398 (1993).
[52]R. Lang and K. Kobayashi, "External optical feedback effects on semiconductor injection laser properties," IEEE Journal of Quantum Electronics **16**, 347–355 (1980).
[53]S. Zhao and F. Grillot, "Effect of Shockley-Read-Hall recombination on the static and dynamical characteristics of epitaxial quantum-dot lasers on silicon," Physical Review A **103**, 063521 (2021).
[54]Y. Deng and C. Wang, "Rate equation modeling of interband cascade lasers on modulation and noise dynamics," IEEE Journal of Quantum Electronics **56**, 1–9 (2020).
[55]F. Grillot, "On the effects of an antireflection coating impairment on the sensitivity to optical feedback of AR/HR semiconductor DFB lasers," IEEE Journal of Quantum Electronics **45**, 720–729 (2009).
[56]J. Ye, H. Li, and J. G. McInerney, "Period-doubling route to chaos in a semiconductor laser with weak optical feedback," Physical Review A **47**, 2249 (1993).
[57]W. Bewley, J. Lindle, C. Kim, M. Kim, C. Canedy, I. Vurgaftman, and J. Meyer, "Lifetimes and Auger coefficients in type-II W interband cascade lasers," Applied Physics Letters **93** (2008).
[58]M. Lerttamrab, S. Chuang, R. Yang, and C. Hill, "Linewidth enhancement factor of a type-II interband-cascade laser," Journal of applied physics **96**, 3568–3570 (2004).
[59]Y. Deng, B.-B. Zhao, and C. Wang, "Linewidth broadening factor of an interband cascade laser," Applied Physics Letters **115** (2019).
[60]L. A. Coldren, S. W. Corzine, and M. L. Mashanovitch, *Diode lasers and photonic integrated circuits*, Vol. 218 (John Wiley & Sons, 2012).
[61]R. Yang, "Mid-infrared interband cascade lasers based on type-II heterostructures," Microelectronics journal **30**, 1043–1056 (1999).
[62]P. Täschler, A. Forrer, M. Bertrand, F. Kapsalidis, M. Beck, and J. Faist, "Asynchronous upconversion sampling of frequency modulated combs," Laser & Photonics Reviews **17**, 2200590 (2023).
[63]P. Didier, H. Dely, T. Bonazzi, O. Spitz, E. Awwad, E. Rodriguez, A. Vasanelli, C. Sirtori, and F. Grillot, "High-capacity free-space optical link in the midinfrared thermal atmospheric windows using unipolar quantum devices," Advanced Photonics **4**, 056004 (2022).
[64]C. L. Canedy, E. M. Jackson, R. L. Espinola, M. R. Pauli, J. M. Auxier, C. S. Kim, M. Kim, J. A. Nolde, C. T. Ellis, E. H. Aifer, *et al.*, "Midwave resonant cavity infrared detectors (RCIDs) with suppressed background noise," Optics Express **31**, 35225–35244 (2023).
[65]Y. Takiguchi, K. Ohyagi, and J. Ohtsubo, "Bandwidth-enhanced chaos synchronization in strongly injection-locked semiconductor lasers with optical feedback," Optics letters **28**, 319–321 (2003).
[66]L. Zhang and S.-C. Chan, "Broadband chaos generation in a distributed-feedback laser by selecting residual side modes," Optics Letters **49**, 1806–1809 (2024).
[67]J. Hillbrand, L. M. Krüger, S. Dal Cin, H. Knötig, J. Heidrich, A. M. Andrews, G. Strasser, U. Keller, and B. Schwarz, "High-speed quantum cascade detector characterized with a mid-infrared femtosecond oscillator," Optics Express **29**, 5774–5781 (2021).
[68]L. Zhang and S.-C. Chan, "Cascaded injection of semiconductor lasers in period-one oscillations for millimeter-wave generation," Optics Letters **44**, 4905–4908 (2019).
[69]X. Pang, A. Caballero, A. Dogadaev, V. Arlunno, R. Borkowski, J. S. Pedersen, L. Deng, F. Karinou, F. Roubeau, D. Zibar, *et al.*, "100 Gbit/s hybrid optical fiber-wireless link in the W-band (75–110 GHz)," Optics express **19**, 24944–24949 (2011).
[70]J.-C. Li, J.-L. Xiao, Y.-D. Yang, Y.-L. Chen, and Y.-Z. Huang, "Random bit generation based on a self-chaotic microlaser with enhanced chaotic bandwidth," Nanophotonics **12**, 4109–4116 (2023).
[71]K. Yang, Y.-L. Chen, Y.-D. Yang, Z.-N. Zhang, J.-L. Xiao, and Y.-Z. Huang, "Nonlinear dynamics in a solitary microlaser based on the interaction between decoupled modes," Journal of Lightwave Technology **42**, 713–720 (2024).
[72]C. E. Shannon, "A mathematical theory of communication," The Bell system technical journal **27**, 379–423 (1948).
[73]J. D. Hart, Y. Terashima, A. Uchida, G. B. Baumgartner, T. E. Murphy, and R. Roy, "Recommendations and illustrations for the evaluation of photonic random number generators," APL Photonics **2**, 090901 (2017).
[74]H. Wu, J. Xiong, B. Han, Z. Wang, W. Zhang, X. Jia, and H. Liang, "Ultra-high speed random bit generation based on Rayleigh feedback assisted ytterbium-doped random fiber laser," Science China Technological Sciences **64**, 1295–1301 (2021).
[75]F. Monet, J.-S. Boisvert, and R. Kashyap, "A simple high-speed random number generator with minimal post-processing using a random Raman fiber laser," Scientific Reports **11**, 1–8 (2021).
[76]B. Shi, C. Luo, J. G. F. Flores, G. Lo, D.-L. Kwong, J. Wu, and C. W. Wong, "Gbps physical random bit generation based on the mesoscopic chaos of a silicon photonics crystal microcavity," Optics Express **28**, 36685–36695 (2020).
[77]C.-H. Tseng, R. Funabashi, K. Kanno, A. Uchida, C.-C. Wei, and S.-K. Hwang, "High-entropy chaos generation using semiconductor lasers subject to intensity-modulated optical injection for certified physical random number generation," Optics Letters **46**, 3384–3387 (2021).
[78]Y. Kawaguchi, T. Okuma, K. Kanno, and A. Uchida, "Entropy rate of chaos in an optically injected semiconductor laser for physical random number generation," Optics Express **29**, 2442–2457 (2021).
[79]Z. Ge, Y. Xiao, T. Hao, W. Li, and M. Li, "Tb/s fast random bit generation based on a broadband random optoelectronic oscillator," IEEE Photonics Technology Letters **33**, 1223–1226 (2021).
[80]K. Wang, Y. Zhang, V. Bheemarasetty, S. Zhou, S.-C. Ying, and G. Xiao, "Single skyrmion true random number generator using local dynamics and interaction between skyrmions," Nature Communications **13**, 1–8 (2022).
[81]Y. Guo, Q. Cai, P. Li, R. Zhang, B. Xu, K. A. Shore, and Y. Wang, "Ultrafast and real-time physical random bit extraction with all-optical quantiza-

tion," Advanced Photonics **4**, 035001 (2022).
[82]B. Cui, G. Xia, X. Tang, Y. Wang, and Z. Wu, "Fast physical random bit generation based on a chaotic optical injection system with multi-path optical feedback," Applied Optics **61**, 8354–8360 (2022).
[83]I. Kanter, Y. Aviad, I. Reidler, E. Cohen, and M. Rosenbluh, "An optical ultrafast random bit generator," Nature Photonics **4**, 58–61 (2010).
[84]Y. Akizawa, T. Yamazaki, A. Uchida, T. Harayama, S. Sunada, K. Arai, K. Yoshimura, and P. Davis, "Fast random number generation with bandwidth-enhanced chaotic semiconductor lasers at 8×50 Gb/s," IEEE Photonics Technology Letters **24**, 1042–1044 (2012).
[85]T. Butler, C. Durkan, D. Goulding, S. Slepneva, B. Kelleher, S. Hegarty, and G. Huyet, "Optical ultrafast random number generation at 1 Tb/s using a turbulent semiconductor ring cavity laser," Optics letters **41**, 388–391 (2016).
[86]J. Soto, "Statistical testing of random number generators," in *Proceedings of the 22nd national information systems security conference*, Vol. 10 (NIST Gaithersburg, MD, 1999) p. 12.
[87]G. Marsaglia and W. W. Tsang, "Some difficult-to-pass tests of randomness," Journal of Statistical Software **7**, 1–9 (2002).